MATERIALS SCIENCE

Enhancing cathode composites with conductive alignment synergy for solid-state batteries

Zhang Cao[1]†, Xinxin Yao[2]†, Soyeon Park[1], Kaiyue Deng[1], Chunyan Zhang[1], Lei Chen[2]*, Kelvin Fu[1]*

Enhancing transport and chemomechanical properties in cathode composites is crucial for the performance of solid-state batteries. Our study introduces the filler-aligned structured thick (FAST) electrode, which notably improves mechanical strength and ionic/electronic conductivity in solid composite cathodes. The FAST electrode incorporates vertically aligned nanoconducting carbon nanotubes within an ion-conducting polymer electrolyte, creating a low-tortuosity electron/ion transport path while strengthening the electrode's structure. This design not only mitigates recrystallization of the polymer electrolyte but also establishes a densified local electric field distribution and accelerates the migration of lithium ions. The FAST electrode showcases outstanding electrochemical performance with lithium iron phosphate as the active material, achieving a high capacity of 148.2 milliampere hours per gram at 0.2 C over 100 cycles with substantial material loading (49.3 milligrams per square centimeter). This innovative electrode design marks a remarkable stride in addressing the challenges of solid-state lithium metal batteries.

INTRODUCTION

Solid-state lithium batteries (SSLBs) are gaining attention in energy storage technology because of their enhanced safety features and increased energy density (*1*–*3*). The development of solid electrolytes and advancements in lithium anode technology have been key to the growth and potential commercialization of SSLBs. However, the production of solid-state composite cathodes faces substantial challenges (*4*, *5*). The selection of solid electrolytes, their complex composition, and the intricate structure of these cathodes, combined with electrode processing, limit lithium-ion transport efficiency in the cathodes (*6*, *7*). These limitations influence charge rates, capacities, and active material utilization efficiency, as well as affect electrode thickness, leading to reduced energy density and overall battery performance.

Addressing the need for cathode architectures that feature reduced fractions of solid electrolytes while improving conductivities and maintaining mechanical stability is paramount. Cathodes incorporating inorganic solid electrolytes typically demonstrate commendable thermal and mechanical stability but are hindered by complex interfacial resistances. Conversely, cathodes using polymer electrolytes may provide improved electrode material contact but are constrained in terms of mechanical properties and operational temperature range. The selection and characteristics of solid electrolytes are influential in determining electrode fabrication methods, thus directly impacting cathode performance. Standard fabrication techniques like thermal compression and slurry casting, using inorganic solid electrolyte powders and polymer electrolytes, respectively, encounter distinct limitations. Thermal compression may limit ion mobility to cathode active materials (CAMs) because of the rigidity of inorganic solid electrolytes, resulting in interfacial impedance and potential degradation of CAMs at elevated sintering temperatures (*8*). Slurry casting with conductive polymers can lead to uneven particle distributions, creating graded tortuosity and residual voids, adversely affecting the cathode's conductivity and chemomechanical integrity (*9*, *10*). Another emerging fabrication technique, the dry process, can achieve high-loading electrodes compared to the traditional slurry casting process. However, the interface contact between electrode materials and solid electrolytes in dry processes is not as good as in slurry casting. Moreover, it is difficult to ensure the uniform distribution of electrode materials in the dry process, especially in electrodes with high loads or complex structures (*10*). This can result in reduced conductivity and ion migration efficiency, ultimately impacting the overall battery performance and hindering the commercial viability of the dry process.

In our study, we introduce an innovative three-dimensional (3D) conducting electrode for solid-state batteries, termed the filler-aligned structured thick (FAST) cathode (Fig. 1A). This design effectively tackles chemomechanical challenges such as limited ion transport efficiency, constrained loading capacity, and high solid electrolyte requirements commonly found in solid composite cathodes. At the core of our design are vertically aligned electron-conducting carbon nanotubes (CNTs), which serve as low-tortuosity conductive scaffolds. These CNTs ensure a uniform distribution of active materials and notably enhance the mechanical strength and conductivity of the cathode. By forgoing solid inorganic ion-conducting fillers and instead using lightweight electron-conducting CNTs, the cathode achieves enhanced ionic conductivity. The CNTs modify the crystallization kinetics of the ion-conducting polymer electrolyte, reducing its crystallinity, while their electric double-layer effect increases the current density on the filler surface, ensuring a densified local electric field. This in turn accelerates the migration speed of lithium ions (Fig. 1B). This strategy moves away from traditional reliance on high-cost, heavy, and complex inorganic electrolytes, adopting a more cost-effective and commonly used polymer electrolyte. Among the numerous polymer electrolyte systems, we use polyethylene oxide (PEO) because it is one of the most widely used polymers because of its advantages such as high lithium salt solubility, easy processing, low cost, and acceptable stability toward lithium metal (*11*, *12*).

The photographic depiction of a structured composite cathode, with a serpentine structure and dimensions of 30 mm by 30 mm by

[1]Department of Mechanical Engineering, University of Delaware, Newark, DE 19716, USA. [2]Department of Mechanical Engineering, University of Michigan, Dearborn, MI 48128, USA.
*Corresponding author. Email: leichn@umich.edu (L.C.); kfu@udel.edu (K.F.)
†These authors contributed equally to this work.

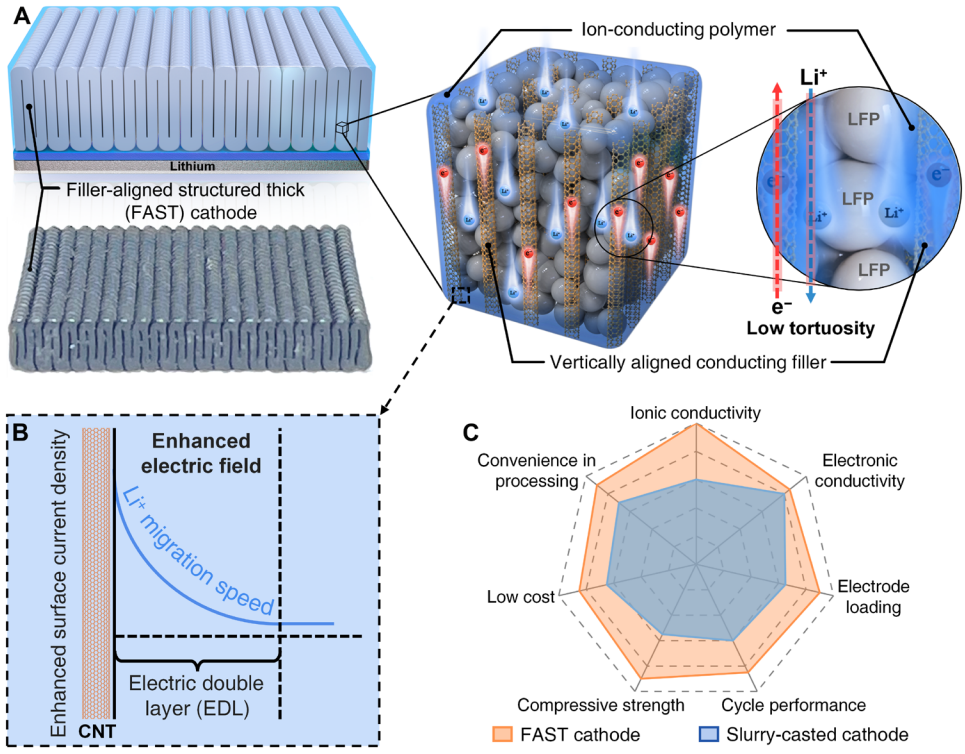

Fig. 1. Structure of the FAST cathode and schematics of the conducting filler effect on the FAST cathode. (**A**) Digital photo of the FAST cathode and schematic of the structure and conduction synergy mechanism of the FAST cathode. (**B**) Schematic of the accelerated ion migration speed under the action of the enhanced electric field in the EDL of the surfaces of conducting fillers in the FAST cathode. (**C**) Comparative analysis illustrating the performance of the FAST cathode relative to a traditionally slurry-casted cathode.

2 mm, is shown in Fig. 1A. The aligned framework of the composite cathode structure is realized through shear-induced alignment during the direct extrusion 3D printing process of the CAM mixture, encompassing CNTs and binder constituents. This approach allows for more convenient and intelligent customization of various geometric structures of electrodes (*13*–*15*). Following this, procedures for binder removal and polymer electrolyte infiltration were undertaken to yield the FAST cathode. The FAST cathode showcases several advantageous characteristics crucial for solid-state batteries, characteristics that are typically challenging to attain with a standard slurry-casted cathode. Figure 1C presents a comparative analysis of seven essential properties of electrodes: ionic conductivity, electronic conductivity, electrode loading, battery cycle performance, compressive strength, cost, and ease of processing. In this comparison, the FAST cathode displays markedly enhanced ionic conductivity (4.25×10^{-4} S/cm at 40°C) and greater loading capacity (49.3 mg/cm^2), substantially outperforming the traditionally slurry-casted cathode in these aspects.

RESULTS

Fabrication process and morphology of the FAST cathode

Figure 2A illustrates the schematic diagram of the fabrication process for the FAST cathode, which involves three distinct stages. Initially, 3D printing technology is used to create the "green" body, consisting of a CNT framework integrated with cathode materials and bound together using a polylactic acid (PLA) binder. This alignment of CNTs is achieved through shear forces during the extrusion printing process. Subsequently, the "green" body undergoes thermal pyrolysis, a process that eliminates PLA and results in the "brown" body [aligned CNT (A-CNT)/LFP]. This stage leaves behind a stable structure comprising CNTs interlocked with the cathode particles, effectively maintaining the electrode's dimensions and the orderly arrangement of CNTs. The final step involves infusing the "brown" body with a polymer electrolyte, specifically PEO-lithium bis(trifluoromethanesulfonyl)imide (PEO-LiTFSI). This in-filtration solidifies the electrode, creating the FAST cathode (A-CNT/LFP/PEO-LiTFSI) that effectively combines the requisite conductive and structural properties for efficient electrochemical performance.

The creation of the "green" body, a critical phase in the process, is shown in Fig. 2B. This stage involves 3D printing using specialized filaments, which are premixed with a proportionate blend of electrode particles and binders. Figure 2C presents the composition of the electrode filament, composed of 60% lithium iron phosphate (LFP), 4% CNTs, 2% carbon black (CB), and 34% PLA polymer (fig. S1). During the extrusion in 3D printing, the CNTs align along the direction of extrusion, driven by high-pressure shear flow (*16*, *17*). Figure 2D displays the "green" body electrode, showcasing its serpentine patterning in each printed layer. This specific pattern ensures the through-thickness alignment of CNTs in the electrodes, vital for the intended structural and conductive properties of the final electrode.

Figure 2E presents a cross-sectional scanning electron microscopy (SEM) image of the "green" body, illustrating a serpentine printing path. This specific pattern is critical as it subjects the CNTs

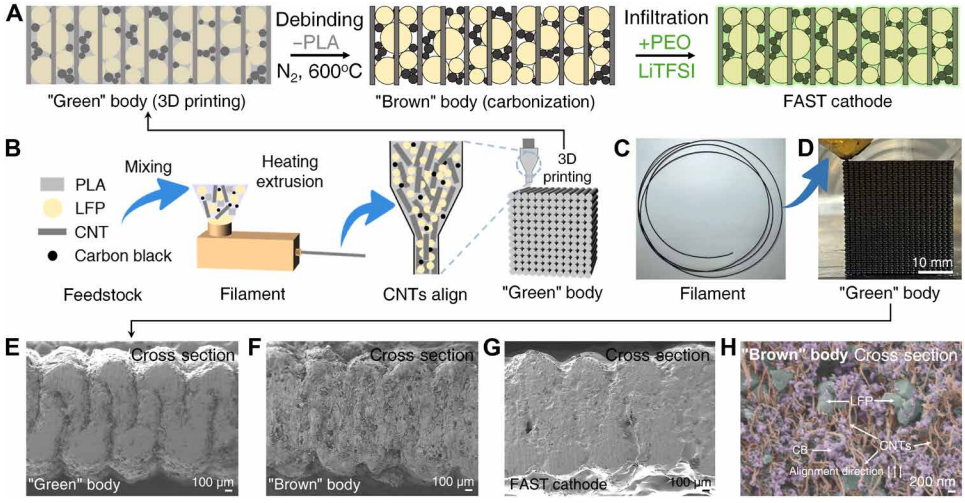

Fig. 2. Fabrication process and morphology of the FAST cathode. (**A**) Illustrated sequence of the FAST cathode's fabrication, depicting stages from "green" and "brown" body formation to polymer electrolyte infiltration. (**B**) Schematic detailing the formation of the electrode filament and subsequent creation of the "green" body electrode. (**C**) Photo of the printable electrode filament. (**D**) Generation of the "green" body electrode through extrusion-based 3D printing. Cross-sectional SEM images illustrating the morphology of the (**E**) "green" body (A-CNT/LFP/PLA) (post-3D printing), (**F**) "brown" body (A-CNT/LFP) (after carbonization), and (**G**) completed FAST cathode (A-CNT/LFP/PEO-LiTFSI) (following polymer electrolyte infiltration). (**H**) SEM image of the colored "brown" body.

to printing shear forces, effectively orienting them to align along the printing direction. This orientation facilitates the through-thickness alignment of CNTs within the cathode. Subsequent thermal pyrolysis at 600°C effectively removes PLA, leaving behind a porous structure composed of LFP and CNTs while preserving the original shape of the "green" body, as shown in Fig. 2F. Figure S2 shows "brown" body (A-CNTs/LFP) SEM images at different magnifications, which distinctly highlight this porous network, featuring aligned CNTs interlocking the LFP particles. Not only can the alignment of CNTs be seen locally, but the distribution of CNT alignment can be seen over a larger area. Figure 2G then reveals the cross section of the FAST cathode, displaying a dense structure achieved by the infiltration of PEO electrolyte into this porous framework (fig. S3). To better visualize the vertically aligned CNT structure within the cathode, the magnified cross-sectional SEM image of the "brown" body is color enhanced (Fig. 2H). Gray indicates LFP, orange-red represents CNTs, and purple-red indicates CB in the color-enhanced SEM image. LFP is evenly distributed among the vertically oriented CNTs, and CB strengthens the connection between the CNTs and LFP. Furthermore, we performed quantitative analysis using Fiji image processing software to assess the degree of alignment of CNTs within the cathode. The alignment factor is determined on the basis of the angular distribution of CNTs relative to the vertical axis, and the results show that the degree of orientation is high, with most CNTs aligned within 20° of the vertical axis (fig. S4). The alignment of CNTs can be characterized more macroscopically by x-ray diffraction (XRD). Figure S5A shows the XRD patterns of PEO-LiTFSI, the FAST cathode, and "brown" body in different orientations. The inset in fig. S5B briefly explains the effect of the alignment direction of CNTs on the (002) peak intensity. When CNTs are aligned vertically, they will be scattered downward by the (002) faces of the vertical CNTs and cannot be detected by the collector. When the CNTs are aligned horizontally, the incident beam is scattered upward, the collector can detect a large amount of the upward scattered beam, and the (002) peak intensity increases. We tested the samples by adjusting the orientation of the "brown" body so that the printing direction was vertical (out-of-plane alignment) and horizontal (in-plane alignment). Comparing the (002) peak intensities of the two samples, the peak intensity of the horizontal "brown" body is obviously greater than that of the vertical "brown" body. This indicates that the CNTs in the FAST cathode are anisotropic and vertically aligned. At the same time, this FAST cathode technology can also be extended to other electrode materials. Figure S6 shows the applicability of FAST technology to the nickel-cobalt-manganese (NCM) cathode.

Structural characterizations of the FAST cathode

Fabricating a thick electrode that retains structural integrity is crucial for improving the energy densities of solid-state batteries, and this is particularly challenging for cathodes containing PEO electrolytes. During the slurry casting process, the drying stage is critical as the removal of solvent can cause particle movement, shrinkage, and cracks within the electrode. Adding fillers like nanoparticles (e.g., Al_2O_3 and garnet-type powders) or nanofibers can strengthen the PEO electrolyte in the electrode, yet the compressive properties across the electrode's thickness are still vulnerable to temperature increases and the pressure exerted by electrode stacking. A FAST cathode featuring an aligned and intertwined CNT framework to encapsulate cathode particles and polymer electrolyte can effectively address these issues found in the slurry-casted cathode. Figure 3A illustrates a comparison between cathodes fabricated using the FAST approach and the slurry casting method (CNT random arrangement), both containing the same composition of PEO electrolyte, CNT, and LFP. The FAST cathode displays an intact structure and robust integrity, with thicknesses up to 200 μm. In contrast, the slurry-casted cathode [random CNT (R-CNT)/LFP/PEO-LiTFSI] shows noticeable cracks, delamination, and uneven thickness across its 200-μm structure (fig. S7). Figure 3B demonstrates the good thermomechanical stability of the FAST cathode, which can withstand

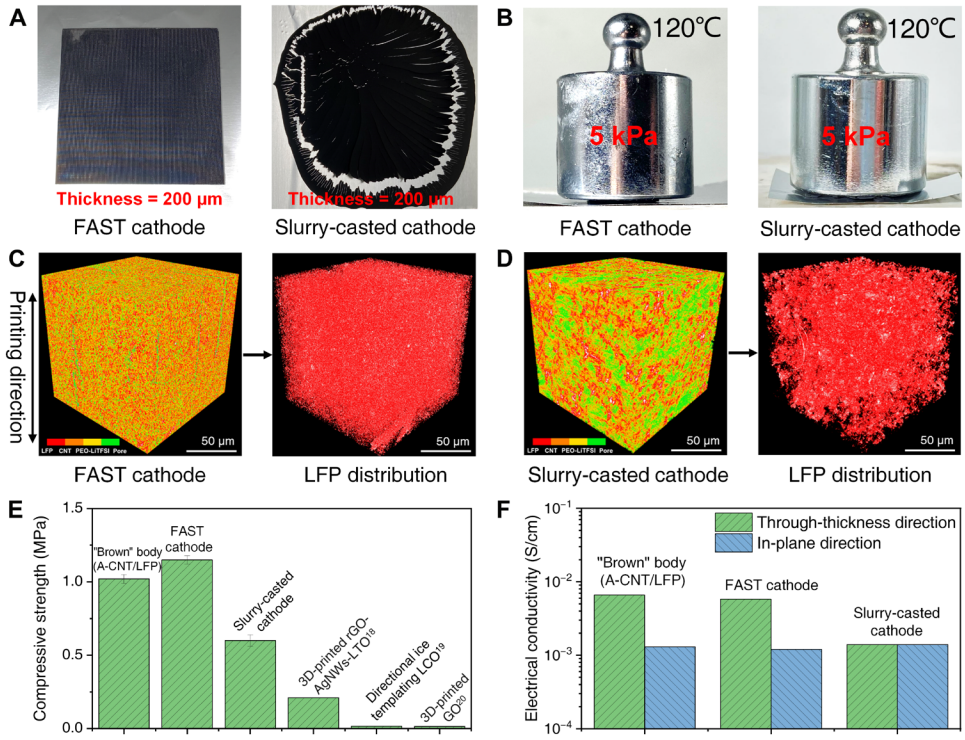

Fig. 3. Structural characterizations of the FAST cathode. (**A**) Thick electrode formability of the FAST and slurry-casted cathodes. (**B**) Thermomechanical stability of the FAST and slurry-casted cathodes under conditions of 120°C and 5-kPa load. Nano-CT images of (**C**) the FAST cathode and (**D**) slurry-casted cathode, with color indications for LFP (red), CNTs (orange), PEO-LiTFSI (yellow), and pores (green). (**E**) Comparative study of the compressive strength between the FAST cathode and thick electrodes typically used with liquid electrolytes (data sourced from the existing literature). rGO, reduced graphene oxide; AgNWs, silver nanowires; LTO, lithium titanium oxide; LCO, lithium cobalt oxide. (**F**) Electrical conductivity comparison between the FAST and slurry-casted cathodes.

temperatures up to 120°C under a 5-kPa load, in contrast to the slurry-casted cathode that compresses and fails to support the same weight under these conditions.

The microstructure of the cathode was further examined using nano–computed tomography (nano-CT). Figure 3 (C and D) displays nano-CT images of the FAST and slurry-casted cathodes, with distinct color coding for various components: red for LFP, orange for CNTs, yellow for the PEO electrolyte, and green representing pores. Notably, aligned green lines are visible, indicative of the aligned channels within the FAST cathode. Extracting the LFP distribution from the CT images reveals a uniform and dense distribution, with a calculated porosity of 17% by volume in the cathode. In contrast, the slurry-casted cathode shows nonuniform distribution of cathode materials, larger pores, and an obviously higher porosity of 32%. In addition, the pore size distribution of the cathodes was measured by mercury intrusion porosimetry (MIP). It can be seen in fig. S8 that the slurry-casted cathode has more micrometer pores, while the FAST cathode has a large reduction in micrometer pores because of the postfilling of the PEO electrolyte. The filled PEO electrolyte is distributed along the CNT, reducing the ionic tortuosity of the cathode. The porosities of slurry-casted and FAST cathodes obtained by MIP are 36.2 and 21.1%, respectively; the trend of the results is consistent with that of nano-CT.

The FAST cathode benefits from the anisotropic properties conferred by the aligned CNTs, which enhance both the compressive strength and electrical conductivity of the cathodes. As shown in Fig. 3E, the "brown" body, constituting the cathode framework before the addition of the PEO electrolyte, already demonstrates commendable compressive strength, reaching up to 1.02 MPa. After the incorporation of PEO electrolytes, the FAST cathode shows a further increase in strength to 1.15 MPa. In addition, the FAST cathode exhibits the highest compressive strength compared to other thick electrodes reported in the literature (*18*–*20*). Figure 3F presents a comparative analysis of the electrical conductivity between the FAST and slurry-casted cathodes. This comparison reveals that the FAST cathode exhibits a higher through-plane electrical conductivity (1.2×10^{-3} S/cm) as compared to its in-plane electrical conductivity (5.8×10^{-3} S/cm). In contrast, the slurry-casted cathode demonstrates a lower overall electrical conductivity (1.4×10^{-3} S/cm), with negligible differences between its in-plane and through-plane conductivities.

Effect of CNTs on the conductivity of the FAST cathode

Figure 4A presents a schematic demonstrating the impact of incorporating aligned CNTs into the FAST cathode with PEO-based polymers on enhancing the cathode's ionic conductivity. The introduction of highly aligned CNTs creates localized amorphous regions at the filler-polymer interface, altering the crystallization kinetics and reducing the crystallinity of PEO. Within these amorphous PEO regions, the uniformly aligned CNTs generate electric double layers (EDLs) around each CNT, densifying the local electric field distribution. This configuration drastically promotes accelerated lithium-ion

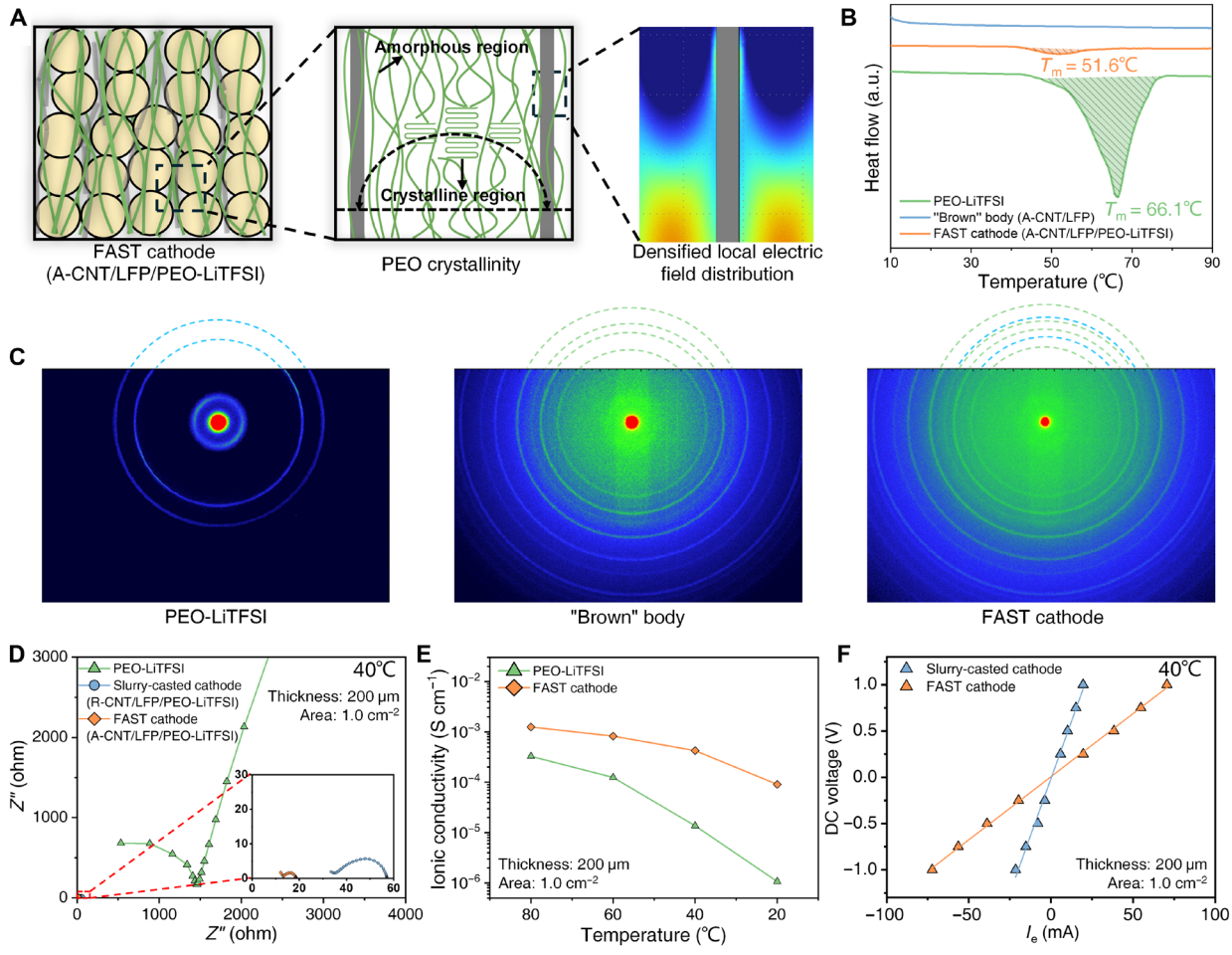

Fig. 4. Effect of CNTs on the conductivity of the FAST cathode. (**A**) Schematic of the effect of CNTs on the FAST cathode (A-CNT/LFP/PEO-LiTFSI). (**B**) DSC of the solid polymer electrolyte (PEO-LiTFSI), "brown" body (A-CNT/LFP), and FAST cathode. (**C**) Two-dimensional wide-angle XRD plots of PEO-LiTFSI, the "brown" body, and FAST cathode. (**D**) EIS tests of PEO-LiTFSI, the slurry-casted cathode, and FAST cathode at 40°C. (**E**) Ionic conductivity at different temperatures of PEO-LiTFSI and FAST cathode. (**F**) DC polarization (V-I_e curves) of the slurry-casted and FAST cathodes at 40°C.

migration along the surfaces of the CNTs. The impact of CNTs on the amorphous state of PEO electrolytes, as determined through experimental studies, along with their effect on local electric field distribution, as analyzed through simulation studies, and the characterization of ionic conductivity are detailed in the following sections. Differential scanning calorimetry (DSC) analysis, as shown in Fig. 4B, was used to ascertain the melting point (T_m) and crystallinity (X_c) of both PEO-LiTFSI and the FAST cathode. Different thermal parameters of PEO-LiTFSI and the FAST cathode are given in table S1. The addition of CNT to PEO-LiTFSI caused a notable reduction in its T_m from 66.1° to 51.6°C, a change indicative of increased amorphization. Amorphous PEO typically has a lower melting point because of its looser molecular structure, requiring less energy to melt. Simultaneously, the melting peak on the DSC curve becomes less pronounced, displaying a broad and gentle endothermic region. This observation also suggests an increased proportion of amorphous PEO. The X_c of the PEO polymer decreases from 44.2% (PEO-LiTFSI) to 15.4% (FAST cathode). This structural alteration suggests potential enhancements in the electrochemical properties of the material, most notably in ionic conductivity. Further investigation into the interaction between the PEO electrolyte and the materials of the FAST cathode was conducted using thermogravimetric (TG) analysis (fig. S9). This analysis revealed that the FAST cathode contains around 12 wt % PEO-LiTFSI compared to its "brown" body. The presence of vertically aligned channels within the FAST cathode facilitates more efficient ion transport, thus allowing for a reduction in the proportion of the PEO-based electrolyte used. Such a reduction is key to enhancing the overall energy density of the battery. Two-dimensional wide-angle x-ray scattering was used to analyze how vertically aligned CNTs affect the crystallization of the PEO electrolyte, as shown in Fig. 4C. The diffraction patterns, highlighted by blue and green circles, indicate the characteristic peaks of the PEO electrolyte (comprising only PEO and LiTFSI) microcrystals and the CNT/LFP mixture. The isotropic ring pattern in the PEO electrolyte film sample suggests an even distribution of crystallites (*21*). In contrast, the FAST cathode maintains its structural integrity and shows minimal characteristic PEO peaks, hinting at a predominantly amorphous state of the polymer. This observation is further validated by 1D XRD analysis (fig. S5A), which also reveals a notable decrease in the crystalline peaks of the PEO electrolyte, affirming the amorphization of PEO (*22*).

Ionic conductivities of the PEO electrolyte, FAST cathode, and slurry-casted cathode were determined from electrochemical impedance

spectroscopy (EIS) measurements, as shown in Fig. 4D. Detailed measurement methods are provided in the Supplementary Materials and fig. S10. The lithium-ion conductivity (σ_i) is calculated using the equation $\sigma_{Li} = L/RS$ (*23*), where *S* is the area of the electrolyte or electrode, *L* represents the thickness of the electrolyte or electrode, and *R* is the ionic resistance obtained from EIS tests with the electrolytes sandwiched between stainless steel plates. At 40°C, the σ_i of the PEO-LiTFSI electrolyte is 1.37×10^{-5} S/cm, which increases to 4.25×10^{-4} S/cm in the FAST cathode (table S2). This important enhancement in σ_i is attributed to the presence of nanofillers (CNTs) within the cathode. Meanwhile, LFP/PEO-LiTFSI with only CB particles was tested (fig. S11). It was found that the ionic conductivity of CB/LFP/PEO-LiTFSI was similar to that of the slurry-casted cathode but less than that of the FAST cathode, which further demonstrated the importance of the vertically aligned structure. The low-tortuosity ion percolation network along the vertical CNTs can reduce the ion diffusion distance in the composite cathode, thereby enhancing the charge transport kinetics (*24*). The ionic tortuosity factor (*k*) of the composite cathode can be estimated using the following equation (Eq. 1)

$$k_i = \frac{\phi_i \sigma_{0,i}}{\sigma_{eff,i}} \quad (1)$$

where ϕ_i represents the volume percentage of the conducting ion phase, $\sigma_{0,i}$ is the ionic conductivity of the pure ionic phase, and $\sigma_{eff,i}$ is the effective ionic conductivity of the composite cathode (*25*). The ionic conductivity of the pure ionic phase ($\sigma_{0,i}$, 40°C) was measured to be 2.54×10^{-3} S/cm (fig. S12), and the *k* value of the FAST cathode was calculated to be 1.5 (table S3). Meanwhile, the value for the slurry-casted cathode is as high as 4.7, which highlights the fact that the FAST cathode has a low-tortuosity ion transport path, resulting in high ion conductivity.

The σ_i of the PEO electrolyte and FAST cathode was tested at different temperatures (Fig. 4E and fig. S13). Temperature has a great influence on the σ_i of the PEO electrolyte, reaching a level that can be used for solid-state batteries at 60°C. Because of the dual influence of CNTs, the FAST cathode can achieve σ_i suitable for solid-state batteries at a lower temperature (40°C). In addition, dc polarization tests were performed to ascertain the stoichiometric intrinsic electronic conductivity (σ_e) of both the FAST and slurry-casted cathodes (Fig. 4F). The slope of the resulting fitted curve represents the electronic resistance, thanks to the vertically aligned CNTs; the σ_e of the FAST cathode (1.47×10^{-3} S/cm) is three times that of the slurry-casted cathode (4.04×10^{-4} S/cm), which is consistent with the results obtained by EIS.

Simulations for local effect demonstration

To delve deeper into how the EDL effect of CNTs contributes to the superior performance of the FAST cathode, finite element simulations are conducted. More details about the simulations can be found in the Supplementary Materials. Figure 5A shows the schematic of how the EDL of CNTs affects the intensity distribution of the electric field, thereby accelerating the migration of lithium ions. Because of the high specific surface area and excellent electrical conductivity of CNTs, the formation of an EDL on the surface of CNT is particularly effective, resulting in an obvious EDL potential V_{EDL} and a strong electric field within the EDL. It should be noted that the electric fields $\mathbf{E}_A$, $\mathbf{E}_{R1}$, and $\mathbf{E}_{R2}$ are the vector superposition of the electric field applied by the battery and the enhanced electric field generated by the CNTs. Compared to randomly distributed CNTs, the vertical arrangement optimizes charge distribution and ensures a more uniform electric field, leading to a drastically greater enhancement of the electric field strength within the EDL. This strengthening effect of the electric field has a dynamic impact on the movement of ions in the electrolyte. The ions in the EDL accelerate their movement, resulting in improved ion migration. To illustrate the effect of CNTs and their arrangement on the ion migration, we design three cases with different CNT distributions, as shown in Fig. 5B. CNTs are represented as cylinders with a length of 23 μm and a cross-sectional radius of 20 nm according to the experiment observation, which are highlighted in blue for better visualization. LFP powder is presented as gray spheres with a size distribution of $D_{50} = 3.5 \pm 1.0$ μm according to experimental data. The dimensions of the simulation domain are 26 μm by 26 μm by 23 μm.

Figure 5C shows the simulation results of the electric field strength contour for the cases of LFP/PEO-LiTFSI, the slurry-casted cathode, and FAST cathode. Compared to LFP/PEO-LiTFSI, the existence of CNT among CAM particles densifies the local electric field (more hotspots) for the slurry-casted cathode because of the double-layer effect of CNT. When CNT distribution becomes aligned (FAST cathode) from a random state (slurry-casted cathode), a more enhanced local electric field is observed. This is because the aligned CNT is conducive to the positive superposition between the electric field applied by the battery and the local enhanced electric field by CNT surfaces, while the randomly distributed CNTs may lead to the mutual attenuation of the electric field in EDL at a specific situation. Figure 5E shows the average electric field strength for three cases and illustrates that the FAST cathode with vertically aligned CNTs has the densest electric field strength (4.4×10^5 V/m). Consequently, the voltage across the cathode for the FAST cathode is higher than those of LFP/PEO-LiTFSI and the slurry-casted cathode, as shown in fig. S14. Figure 5D depicts the simulation results of the lithium-ion concentration distribution for different cases after 4 s, demonstrating how the enhanced electric field promotes the ion migration. The lithium-ion movement is driven by both the electric field and concentration gradient diffusion. It is evident that, compared to LFP/PEO-LiTFSI without CNTs, lithium-ion dynamics are more rapid in the presence of CNTs, as seen in the slurry-casted and FAST cathodes. The local electric field near the CNT surface drastically enhances ion movement, with the FAST cathode showing the most rapid change. Figure 5F depicts the simulation results of average lithium-ion concentration changes with time for different cases. The green curve represents the effect of aligned CNTs (FAST cathode) on lithium-ion variation, the blue curve indicates the impact of R-CNTs (slurry-casted cathode) on lithium-ion variation, and the red curve shows the lithium-ion variation in the absence of CNTs. With the addition of CNTs, the enhanced electric field accelerates the migration of lithium ions. In addition, the addition of vertically aligned CNTs can lead to the formation of faster lithium-ion channels. Consequently, the incorporation of aligned CNTs into the FAST cathode structure not only results in a more efficient electric field distribution but also drastically enhances the transport efficiency of lithium ions. To investigate the effect of the surface charge density ρ_{s2} of CNTs on lithium-ion transportation, the simulation results of the average migration velocity at different ρ_{s2} values were compared with the experimental ionic conductivity (Fig. 5G). It can be clearly seen that the ion migration velocity increases with the

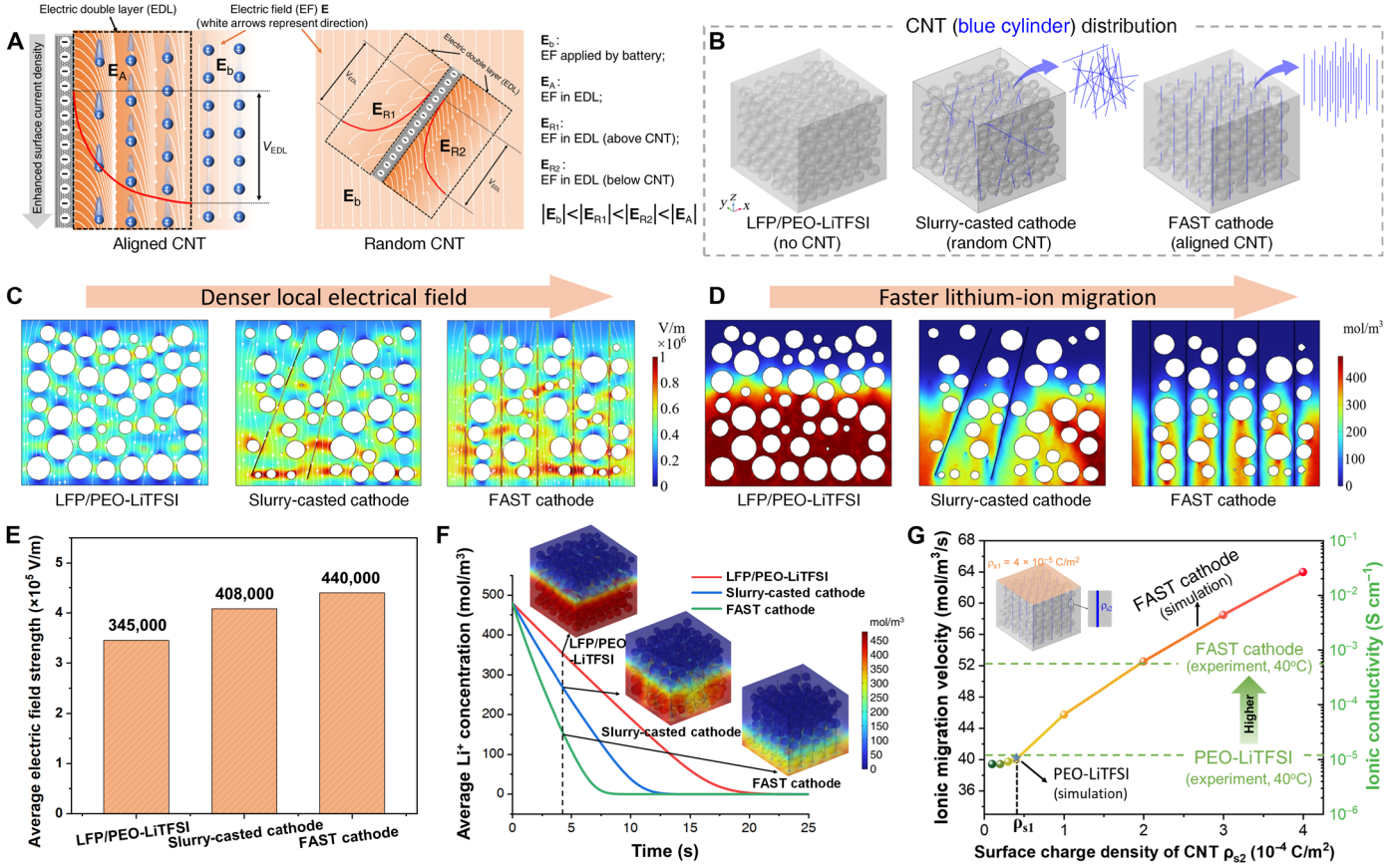

Fig. 5. Simulations for local effect demonstration. (**A**) Schematic of the effect of the EDL of CNTs on electric field distribution and ion migration speed. Accelerated migration speed can be observed under the high electric field intensity in the EDL as a result of the enhanced surface current density of A-CNTs. (**B**) Geometries for LFP/PEO-LiTFSI, slurry-casted cathode, and FAST cathode. a.u., arbitrary units. (**C**) Simulations for electric field distribution for LFP/PEO-LiTFSI, the slurry-casted cathode, and FAST cathode. (**D**) Simulations for lithium-ion concentration distribution for LFP/PEO-LiTFSI, the slurry-casted cathode, and FAST cathode after 4 seconds. (**E**) Average electric field strength for LFP/PEO-LiTFSI, the slurry-casted cathode, and FAST cathode. (**F**) Simulation result of average lithium-ion concentration changes with time for LFP/PEO-LiTFSI, the slurry-casted cathode, and FAST cathode. (**G**) Comparison between simulated results of average migration velocity under different ρ_{s2} values and experimental ionic conductivities. S, seconds.

increase in the surface charge density ρ_{s2} of CNTs. The quantitative comparison of the ionic conductivity between experiments and simulations confirms the conclusion that the high surface charge density of CNTs is the reason for the excellent transport efficiency.

Demonstration of solid-state Li metal batteries using the FAST and slurry-casted cathodes

To identify the feasibility of the cathode architecture design, LFP/PEO/Li cells with FAST and slurry-casted cathodes were assembled and evaluated. Cyclic voltammetry (CV) test was used to characterize the electrochemical kinetics of cathodes. Figure 6A displays the CV curves of slurry-casted and FAST cathodes at a scan rate of 0.1 mV/s; the peaks at 3.6 and 3.3 V in the positive and negative scans correspond to the lithium extraction and insertion processes into the LFP host (*26*). The peak in the FAST cathode is narrower and higher than that in the slurry-casted cathode, which indicates that the FAST cathode has better electrochemical kinetic behavior. In the conventional slurry-casted cathode, the peaks become lower and broader, and the peak in the negative scan shifts toward higher voltages, indicating a large impedance, mainly because of the slow diffusion of lithium ions in the cathode.

EIS was performed in solid-state cells using slurry-casted and FAST cathodes after 100 cycles, as shown in Fig. 6B. The overall impedance of the cell using the FAST cathode is approximately 891.5 ohms, which is much lower than 6584 ohms of the cell using the slurry-casted cathode. The straight line of the impedance spectrum in the low-frequency band mainly reflects the "ion transport properties" of the electrochemical reaction. The slope of the straight line is related to the migration rate of ions in the cathode. That is, the steeper the slope, the higher the ion migration rate and the better the ion conductivity of the cell. The cell with the FAST cathode benefits from low-tortuosity ion channels, resulting in drastically higher migration speed of lithium ions than cells with slurry-casted cathodes with randomly arranged high-tortuosity ion channels. The rate capabilities of the FAST and slurry-casted cathodes were evaluated at varying rates from 0.1 to 5 C at 40°C, as shown in Fig. 6C. Under high–active material loading conditions, the FAST cathode demonstrates more pronounced performance advantages at higher rates compared to the slurry-casted cathodes. Its unique vertical structure design ensures stable operation even at a high current density of 1 C. Figure 6 (D and E) illustrates the initial charge/discharge profiles of both FAST and slurry-casted cathodes at different current

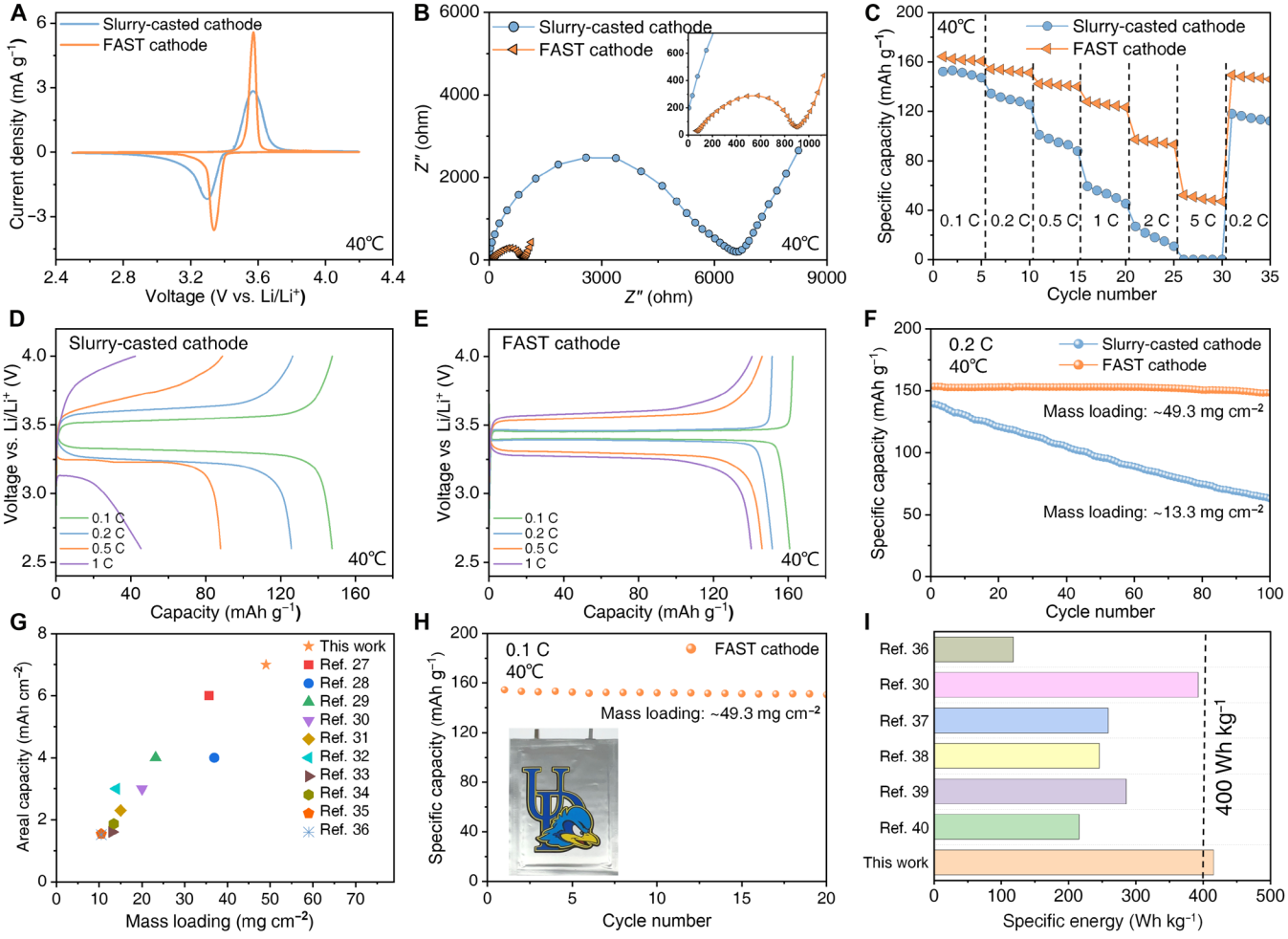

Fig. 6. Demonstration of solid-state Li metal batteries using the FAST and slurry-casted cathodes at 40°C. (**A**) CV curves of the slurry-casted and FAST cathodes. (**B**) EIS curves of the slurry-casted and FAST cathodes after 100 cycles. (**C**) Rate performance of the slurry-casted and FAST cathodes at different current densities. (**D** and **E**) Charge-discharge profiles of the slurry-casted and FAST cathodes at increasing current densities. (**F**) Long-term cycling of the slurry-casted and FAST cathodes at 0.2 C. (**G**) Comparison of cathode areal capacities (plotted as a function of CAM loading) of various studies. (**H**) Electrochemical performance of the LFP/PEO/Li pouch cell using the FAST cathode at 0.1 C. (**I**) Energy density comparison of related work.

densities. The discharge capacities were recorded at 147.3 mAh/g for the slurry-casted cathode and 160.7 mAh/g for the FAST cathode at 0.1 C. Notably, the capacity of the slurry-casted cathode decreases rapidly with increasing current density, a decline attributed to its lower ionic conductivity.

Differences in LFP/Li cells with various cathodes over 100 cycles at 0.2 C are further depicted in Fig. 6F. The capacity of the slurry-casted cathode experiences a sharp decline, dropping to ~62.8 mAh/g after 100 cycles. In contrast, the FAST cathode exhibits a consistent increase in capacity over all cycles, maintaining a specific capacity of 148.2 mAh/g after 100 cycles at 0.2 C, with a material loading of 49.3 mg/cm^2. Figure S15 shows that the coulombic efficiency of the FAST cathode is more stable than the slurry-casted cathode. The vertical structure of the FAST cathode minimizes the impact of thickness on ion diffusion paths, allowing for the full and effective utilization of active materials. The loading and areal capacity of this study outperform those of previously reported SSLBs (Fig. 6G) (*27*–*36*). The high energy density of the FAST cathode was verified by assembling a double-layer pouch cell made of LFP/PEO/Li (fig. S16). A reversible discharge capacity of 153 mAh/g was achieved at 0.1 C and 40°C (Fig. 6H). In addition, a comparison of the energy density of our FAST cathode with that of other reported high-load cathodes (Fig. 6I) (*30*, *36*–*40*) reveals that our designed 3D vertical conductive electrode structure battery achieves a cathode energy density exceeding 400 Wh/kg, surpassing other SSLBs because of its high loading and ionic conductivity.

DISCUSSION

In this study, we introduce a transformative 3D conducting cathode for SSLBs, named the FAST cathode. This design effectively addresses prevalent issues in solid composite cathodes, such as inefficient ion transport and limited loading capacity. Central to the FAST electrode's innovation is the integration of vertically aligned CNTs. These CNTs act as conductive scaffolds, enhancing mechanical strength while ensuring low-tortuosity pathways for electron and ion transport, notably improving both ionic and electronic conductivities. In addition, they establish a densified local electric

field, markedly boosting ion migration and enhancing the cathode's dielectric properties. Demonstrating robust electrochemical performance, the FAST cathode achieves 148.2 mAh/g at 0.2 C over 100 cycles with a material loading of 49.2 mg/cm^2 at 40°C. This adaptable design, compatible with a range of cathode materials, conducting fillers, and solid polymer electrolytes, marks a remarkable advancement in the field of solid-state lithium metal batteries.

MATERIALS AND METHODS

Materials

Battery-grade Li salts of LiTFSI, PEO (molecular weight ≥ 300,000), and acetonitrile were obtained from Sigma-Aldrich (St. Louis, MO, USA). The CNTs (10 to 30 μm in length) purchased from Cheap Tubes (Grafton, VT, USA) were used to fabricate the carbonizable filament. The CNTs were randomly oriented in the powder, and the powder was sealed and stored in a drying oven. The CB powder (average diameter, 30 nm), commercial LFP powder (particle size, D_{50} = 3.5 ± 1.0 μm), and commercial NCM powder (particle size, D_{50}: 11 ± 2 μm) were purchased from MTI Corporation. The PLA granule and dichloromethane (DCM) were purchased from Filabot (Barre, VT, USA) and Sigma-Aldrich (St. Louis, MO, USA), respectively, and used as received without further purification.

Preparation of the electrode filament

A slurry was made by dissolving the PLA polymer into DCM. Once PLA was fully melted, the fillers, including active materials, were added and mixed overnight. The weight ratio of components for the electrode filament was 34/60/4/2 (PLA/LFP/CNT/CB). The dried composite was cut into small pieces to facilitate extrusion. The electrode filament with ≈1.75-mm diameter was extruded at 175°C through a single extruder (CarbonForm Inc.).

FAST cathode preparation

The zigzag structure electrodes (CNT vertically aligned cathodes) were printed using a fused deposition modeling printer (CarbonForm Inc.). They were printed out at 195°C with 10-mm/s speed using a 0.4-mm nozzle. The top and bottom sides of the printed electrodes were sanded using sandpaper of different grain sizes (3M; 400 and 3000) to suit electrode thicknesses of ~0.2 and ~0.4 mm. They were placed on the copper foil, which is used as a current collector, and attached using the heat of the hot plate (~80°C). The electrodes with the current collector were carbonized at 600°C in nitrogen for 2 hours using the MTI tube furnace to obtain the "brown" body. PEO was mixed with LiTFSI (Li:EO = 1:32) and acetonitrile using a Thinky mixer to form a homogeneous PEO-based electrolyte solution. Then, the PEO-LiTFSI electrolyte was filled into the "brown" body, dried in a vacuum oven at 40°C for 24 hours to remove most of the acetonitrile solvent, and continued to be vacuum dried at 50°C for 48 hours to completely evaporate the acetonitrile solvent to obtain the FAST cathode. To obtain the highest-performance battery, without reducing the utilization of LFP, the cathode thickness used is 300 μm.

Slurry-casted cathode preparation

LFP powders, PEO-LiTFSI, CNTs, and CB at a weight ratio of 80:12:5.3:2.7 were mixed in acetonitrile to form a uniform slurry using a Thinky mixer. The slurry was then doctoring blade casted on Al foil. The cathode was then dried in a 60°C vacuum oven for at least 48 hours. To ensure the normal operation of the battery, the slurry-casted cathode thickness used is 100 μm, with an LFP active material loading of 13.3 mg cm^{-2}.

Assembly of solid-state batteries

The solid-state batteries were assembled in an argon-filled glovebox. The coin cell (CR2032) was made with a Li-metal anode, polyacrylonitrile (PAN)–PEO-LiTFSI polymer electrolyte membrane, and cathode (FAST and slurry-casted cathodes made as described above). The thickness of the lithium anode used in the experiment is 0.137 mm. The LFP/PAN-PEO-LiTFSI/Li pouch cell is assembled with trilayer design. For one pouch cell, the size of the FAST cathode is designed to be 90 mm by 65 mm, with a cathode mass loading of 49.3 mg/cm^2. Two pieces of thin Li (137 μm) have been double coated on a piece of Cu current collector (8 μm) by pressing. The thickness of the PAN-PEO-LiTFSI polymer electrolyte membrane is 60 μm. Because the FAST cathode is very thick, the number of cathode layers used in the test can be greatly reduced to reduce the ratio of the current collector to the membrane and improve the battery energy density.

Supplementary Materials

This PDF file includes:

Supplementary Text
Figs. S1 to S19
Tables S1 to S3
References

REFERENCES AND NOTES

1. J. Kang, N. Deng, Y. Liu, Z. Yan, L. Gao, H. Xiang, L. Zhang, G. Wang, B. Cheng, W. Kang, Recent advances of anode protection in solid-state lithium metal batteries. *Energy Storage Mater.* **52**, 130–160 (2022).
2. L. Li, Y. Deng, G. Chen, Status and prospect of garnet/polymer solid composite electrolytes for all-solid-state lithium batteries. *J. Energy Chem.* **50**, 154–177 (2020).
3. A. Cronk, Y.-T. Chen, G. Deysher, S.-Y. Ham, H. Yang, P. Ridley, B. Sayahpour, L. H. B. Nguyen, J. A. S. Oh, J. Jang, D. H. S. Tan, Y. S. Meng, Overcoming the interfacial challenges of $LiFePO_4$ in inorganic all-solid-state batteries. *ACS Energy Lett.* **8**, 827–835 (2023).
4. W. Zhang, D. A. Weber, H. Weigand, T. Arlt, I. Manke, D. Schröder, R. Koerver, T. Leichtweiss, P. Hartmann, W. G. Zeier, J. Janek, Interfacial processes and influence of composite cathode microstructure controlling the performance of all-solid-state lithium batteries. *ACS Appl. Mater. Inter.* **9**, 17835–17845 (2017).
5. Y. Sakka, H. Yamashige, A. Watanabe, A. Takeuchi, M. Uesugi, K. Uesugi, Y. Orikasa, Pressure dependence on the three-dimensional structure of a composite electrode in an all-solid-state battery. *J. Mater. Chem. A* **10**, 16602–16609 (2022).
6. J. Ma, G. Zhong, P. Shi, Y. Wei, K. Li, L. Chen, X. Hao, Q. Li, K. Yang, C. Wang, W. Lv, Q.-H. Yang, Y.-B. He, F. Kang, Constructing a highly efficient "solid–polymer–solid" elastic ion transport network in cathodes activates the room temperature performance of all-solid-state lithium batteries. *Energ. Environ. Sci.* **15**, 1503–1511 (2022).
7. Y. Yuan, L. Chen, Y. Li, X. An, J. Lv, S. Guo, X. Cheng, Y. Zhao, M. Liu, Y.-B. He, F. Kang, Functional $LiTaO_3$ filler with tandem conductivity and ferroelectricity for PVDF-based composite solid-state electrolyte. *Energy Mater. Dev.* **1**, 9370004 (2023).
8. J. Haruyama, K. Sodeyama, L. Han, K. Takada, Y. Tateyama, Space–charge layer effect at interface between oxide cathode and sulfide electrolyte in all-solid-state lithium-ion battery. *Chem. Mater.* **26**, 4248–4255 (2014).
9. W. Yao, M. Chouchane, W. Li, S. Bai, Z. Liu, L. Li, A. X. Chen, B. Sayahpour, R. Shimizu, G. Raghavendran, M. A. Schroeder, Y.-T. Chen, D. H. S. Tan, B. Sreenarayanan, C. K. Waters, A. Sichler, B. Gould, D. J. Kountz, D. J. Lipomi, M. Zhang, Y. Shirley Meng, A 5 V-class cobalt-free battery cathode with high loading enabled by dry coating. *Energ. Environ. Sci.* **16**, 1620–1630 (2023).
10. Y. Lu, C.-Z. Zhao, H. Yuan, J.-K. Hu, J.-Q. Huang, Q. Zhang, Dry electrode technology, the rising star in solid-state battery industrialization. *Matter* **5**, 876–898 (2022).
11. G. S. MacGlashan, Y. G. Andreev, P. G. Bruce, Structure of the polymer electrolyte poly(ethylene oxide)$_6$:$LiAsF_6$. *Nature* **398**, 792–794 (1999).
12. L. Long, S. Wang, M. Xiao, Y. Meng, Polymer electrolytes for lithium polymer batteries. *J. Mater. Chem. A* **4**, 10038–10069 (2016).

13. W. Ping, C. Wang, R. Wang, Q. Dong, Z. Lin, A. H. Brozena, J. Dai, J. Luo, L. Hu, Printable, high-performance solid-state electrolyte films. *Sci. Adv.* **6**, eabc8641 (2020).
14. S. Zhou, M. Li, P. Wang, L. Cheng, L. Chen, Y. Huang, S. Yu, F. Mo, J. Wei, Printed solid-state batteries. *Electrochem. Energy Rev.* **6**, 34 (2023).
15. X. Shi, Z.-S. Wu, X. Bao, Recent advancements and perspective of high-performance printed power sources with multiple form factors. *Electrochem. Energ. Rev.* **3**, 581–612 (2020).
16. H. Guo, H. Zhao, H. Niu, Y. Ren, H. Fang, X. Fang, R. Lv, M. Maqbool, S. Bai, Highly thermally conductive 3D printed graphene filled polymer composites for scalable thermal management applications. *ACS Nano* **15**, 6917–6928 (2021).
17. S. Park, B. Shi, Y. Shang, K. Deng, K. Fu, Structured electrode additive manufacturing for lithium-ion batteries. *Nano Lett.* **22**, 9462–9469 (2022).
18. C. Sun, S. Liu, X. Shi, C. Lai, J. Liang, Y. Chen, 3D printing nanocomposite gel-based thick electrode enabling both high areal capacity and rate performance for lithium-ion battery. *Chem. Eng. J.* **381**, 122641 (2020).
19. C. Huang, P. S. Grant, Coral-like directional porosity lithium ion battery cathodes by ice templating. *J. Mater. Chem. A* **6**, 14689–14699 (2018).
20. X. Tang, H. Zhou, Z. Cai, D. Cheng, P. He, P. Xie, D. Zhang, T. Fan, Generalized 3D printing of graphene-based mixed-dimensional hybrid aerogels. *ACS Nano* **12**, 3502–3511 (2018).
21. M. A. Browe, J. Landers, T. M. Tovar, J. J. Mahle, A. Balboa, W. O. Gordon, M. Fukuto, C. J. Karwacki, Laponite-incorporated UiO-66-NH_2-polyethylene oxide composite membranes for protection against chemical warfare agent simulants. *ACS Appl. Mater. Inter.* **13**, 10500–10512 (2021).
22. N. Zhang, J. He, W. Han, Y. Wang, Composite solid electrolyte PEO/SN/$LiAlO_2$ for a solid-state lithium battery. *J. Mater. Sci.* **54**, 9603–9612 (2019).
23. W. Liu, N. Liu, J. Sun, P.-C. Hsu, Y. Li, H.-W. Lee, Y. Cui, Ionic conductivity enhancement of polymer electrolytes with ceramic nanowire fillers. *Nano Lett.* **15**, 2740–2745 (2015).
24. L. Li, R. M. Erb, J. Wang, J. Wang, Y.-M. Chiang, Fabrication of low-tortuosity ultrahigh-area-capacity battery electrodes through magnetic alignment of emulsion-based slurries. *Adv. Energy Mater.* **9**, 1802472 (2019).
25. M. Rana, Y. Rudel, P. Heuer, E. Schlautmann, C. Rosenbach, M. Y. Ali, H. Wiggers, A. Bielefeld, W. G. Zeier, Toward achieving high areal capacity in silicon-based solid-state battery anodes: What influences the rate-performance? *ACS Energy Lett.* **8**, 3196–3203 (2023).
26. K. Tang, X. Yu, J. Sun, H. Li, X. Huang, Kinetic analysis on $LiFePO_4$ thin films by CV, GITT, and EIS. *Electrochim. Acta* **56**, 4869–4875 (2011).
27. K. Wang, Z. Liang, S. Weng, Y. Ding, Y. Su, Y. Wu, H. Zhong, A. Fu, Y. Sun, M. Luo, J. Yan, X. Wang, Y. Yang, Surface engineering strategy enables 4.5 V sulfide-based all-solid-state batteries with high cathode loading and long cycle life. *ACS Energy Lett.* **8**, 3450–3459 (2023).
28. Z. Li, Z. Wang, Y. Miao, Y. Ma, H. Zhang, X. Shi, D. Song, L. Zhang, L. Zhu, Constructing rapid ionic transfer layer to boost the performance of $LiCoO_2$ cathode with high mass loading for all-solid-state lithium battery. *J. Power Sources* **541**, 231703 (2022).
29. X. Li, W. Peng, R. Tian, D. Song, Z. Wang, H. Zhang, L. Zhu, L. Zhang, Excellent performance single-crystal NCM cathode under high mass loading for all-solid-state lithium batteries. *Electrochim. Acta* **363**, 137185 (2020).
30. G. Cheng, H. Sun, H. Wang, Z. Ju, Y. Zhu, W. Tian, J. Chen, H. Wang, J. Wu, G. Yu, Efficient ion percolating network for high-performance all-solid-state cathodes. *Adv. Mater.* **36**, 2312927 (2024).
31. Y. Liu, X. An, K. Yang, J. Ma, J. Mi, D. Zhang, X. Cheng, Y. Li, Y. Ma, M. Liu, F. Kang, Y.-B. He, Achieving a high loading of cathode in PVDF-based solid-state battery. *Energ. Environ. Sci.* **17**, 344–353 (2024).
32. X. Gao, B. Liu, B. Hu, Z. Ning, D. S. Jolly, S. Zhang, J. Perera, J. Bu, J. Liu, C. Doerrer, E. Darnbrough, D. Armstrong, P. S. Grant, P. G. Bruce, Solid-state lithium battery cathodes operating at low pressures. *Joule* **6**, 636–646 (2022).
33. Y. Lin, M. Wu, J. Sun, L. Zhang, Q. Jian, T. Zhao, A high-capacity, long-cycling all-solid-state lithium battery enabled by integrated cathode/ultrathin solid electrolyte. *Adv. Energy Mater.* **11**, 2101612 (2021).
34. L. Nie, R. Gao, M. Zhang, Y. Zhu, X. Wu, Z. Lao, G. Zhou, Integration of porous high-loading electrode and gel polymer electrolyte for high-performance quasi-solid-state battery. *Adv. Energy Mater.* **14**, 2302476 (2024).
35. B. Zhang, L. Chen, J. Hu, Y. Liu, Y. Liu, Q. Feng, G. Zhu, L.-Z. Fan, Solid-state lithium metal batteries enabled with high loading composite cathode materials and ceramic-based composite electrolytes. *J. Power Sources* **442**, 227230 (2019).
36. X. Yang, Q. Sun, C. Zhao, X. Gao, K. R. Adair, Y. Liu, J. Luo, X. Lin, J. Liang, H. Huang, L. Zhang, R. Yang, S. Lu, R. Li, X. Sun, High-areal-capacity all-solid-state lithium batteries enabled by rational design of fast ion transport channels in vertically-aligned composite polymer electrodes. *Nano Energy* **61**, 567–575 (2019).
37. Y. Ouyang, W. Gong, Q. Zhang, J. Wang, S. Guo, Y. Xiao, D. Li, C. Wang, X. Sun, C. Wang, S. Huang, Bilayer zwitterionic metal-organic framework for selective all-solid-state superionic conduction in lithium metal batteries. *Adv. Mater.* **35**, e2304685 (2023).
38. J. Wan, J. Xie, X. Kong, Z. Liu, K. Liu, F. Shi, A. Pei, H. Chen, W. Chen, J. Chen, X. Zhang, L. Zong, J. Wang, L.-Q. Chen, J. Qin, Y. Cui, Ultrathin, flexible, solid polymer composite electrolyte enabled with aligned nanoporous host for lithium batteries. *Nat. Nanotechnol.* **14**, 705–711 (2019).
39. H. Li, F. Lian, N. Meng, C. Xiong, N. Wu, B. Xu, Y. Li, Constructing electronic and ionic dual conductive polymeric interface in the cathode for high-energy-density solid-state batteries. *Adv. Funct. Mater.* **31**, 2008487 (2021).
40. J. Wu, Z. Rao, Z. Cheng, L. Yuan, Z. Li, Y. Huang, Ultrathin, flexible polymer electrolyte for cost-effective fabrication of all-solid-state lithium metal batteries. *Adv. Energy Mater.* **9**, 1902767 (2019).
41. S. Klongkan, J. Pumchusak, Effects of nano alumina and plasticizers on morphology, ionic conductivity, thermal and mechanical properties of PEO-$LiCF_3SO_3$ solid polymer electrolyte. *Electrochim. Acta* **161**, 171–176 (2015).
42. R. A. Huggins, Simple method to determine electronic and ionic components of the conductivity in mixed conductors a review. *Ionics* **8**, 300–313 (2002).
43. W. Zhang, H. Xiong, S. Wang, M. Li, Y. Gu, Electromagnetic characteristics of carbon nanotube film materials. *Chinese J. Aeronaut* **28**, 1245–1254 (2015).
44. J. Lyklema, M. Minor, On surface conduction and its role in electrokinetics. *Colloid Surface A* **140**, 33–41 (1998).

Acknowledgments

Funding: This work was funded by the University of Delaware start-up. K.F. acknowledges financial support by the US Department of Energy (DoE) under grant DE-FE0032147.

Author contributions: Z.C. conceived and designed the experiment, performed the battery experiment, performed SEM, analyzed the data, and led and revised writing. X.Y. designed simulation methods, analyzed data, and revised writing. S.P., K.D., and C.Z. performed TG, nano-CT, and XRD experiments. L.C. designed simulation methods and discussed and commented on the manuscript. K.F. supervised the overall direction of the experiment and discussed and commented on the manuscript. **Competing interests:** The authors declare that they have no competing interests. **Data and materials availability:** All data needed to evaluate the conclusions in the paper are present in the paper and/or the Supplementary Materials.

Submitted 2 July 2024
Accepted 2 December 2024
Published 3 January 2025
10.1126/sciadv.adr4292